RSC Advances

PAPER

View Article Online
View Journal | View Issue

Cite this: *RSC Adv.*, 2014, **4**, 22

Revised electronic structure, Raman and IR studies of AB_2H_2 and $ABCH$ (A = Sr, Ba; B = Al, Ga; C = Si, Ge) phases†

P. Vajeeston* and H. Fjellvåg

Received 8th August 2013
Accepted 22nd October 2013

DOI: 10.1039/c3ra44248a

www.rsc.org/advances

Modern density functional theory (DFT) provides an extremely valuable tool for predicting structures and energetics of new materials for both finite and periodic systems. In the present work the electronic structure, chemical bonding, and spectroscopic properties of AB_2H_2, and $ABCH$ (A = Sr, Ba; B = Al, Ga; C = Si, Ge) phases have been studied by state-of-the-art density-functional calculations. In contrast with the previous theoretical studies, present electronic structures calculation using hybrid B3LYP reveal that AB_2H_2, phases are indirect bandgap semiconductors with estimated bandgap vary from 0.324 to 0.495 eV. In general, B3LYP gives a reasonable description of the electronic structure of semiconductors, semi-ionic oxides, sulfides, transition metal oxides and the ionic oxide. Similar to the AB_2H_2 phases $ABCH$ phases are also indirect bandgap semiconductors and the magnitude is much higher than for the AB_2H_2 phases. We have also simulated the Raman and IR spectra, and calculated the NMR related parameters such as isotropic chemical shielding, quadrupolar coupling constant, and quadrupolar asymmetry for the AB_2H_2, and $ABCH$ phases.

Introduction

The current interest in the development of novel metal hydride systems are due to their potential use as a reversible hydrogen storage application at low and medium temperatures. Various aluminum based hydrides such as catalyzed sodium alanate have been recently studied for this purpose. The studies of hydrides have so far been focused on the acceleration of kinetics for the hydrogenation/dehydrogenation processes at moderate temperatures and on the increase of the weight percentage of hydrogen. So those hydrides characterized by relatively slow kinetics for hydrogenation/dehydrogenation processes and high decomposition temperature are not interesting for hydrogen economy. However, these hydrides have recently been suggested to find unique exciting applications in optoelectronics.[1] But the proposed applications depend on their stability with respect to doping, solubility of shallow donors and acceptors, and electrical as well as optical properties. Furthermore, the hydrides are widely available in powder form, which is required for hydrogen storage/economy, but is not preferable for electronic device technology. For the latter applications crystalline or amorphous hydrides are more preferable. It should be noted that single crystals of SrAlSi are transformed into identically shaped crystals of the hydrogenated SrAlSiH product and they can be exposed to air and moisture without any decomposition.[2]

In 2000 Gingl *et al.* reported the synthesis and structural characterization of the novel compound $SrAl_2H_2$.[3] Contrary to the alanates $A_mAe_nAl_oH_{m+2n+3o}$ (A, Ae = alkali and alkaline-earth metal, respectively), this aluminum hydride is not fully hydrogenated and was described as a "Zintl phase hydride". It features a two-dimensional $[Al_2H_2]^{2-}$ polyanion in which the Al atoms are arranged as a puckered graphitic layer with three nearest neighbors.[3] The vacant coordination site is taken by hydrogen and the compound appears to be charge-balanced. The hydrogen content of this hydride is comparably low, and thus they may not be appropriate as hydrogen storage materials. However, if physical properties inherent to saline metal hydrides and Zintl phases can be combined in polyanionic hydride, unexpected prospects are opened and the hydride materials research is then extended beyond the traditional quest for hydrogen storage materials.[2] The structure of SrAlSiH is very similar to that of $SrAl_2H_2$, half of the Al–H entities in the 2D polyanionic layer of $SrAl_2H_2$ are replaced by isoelectronic Si.[2] It is important to note that superconducting AlB_2-type silicides CaAlSi, SrAlSi, and BaAlSi absorb hydrogen and form semiconducting monohydrides where hydrogen is exclusively attached to Al. Similarly SrAlGe, BaAlGe, BaGaSi, and BaGaGe are also stabilized in AlB_2-type structure.[4,5] In general, Zintl phases are a subgroup of brittle, high melting point intermetallic compounds which are diamagnetic or exhibit temperature-independent *para*-magnetism, and are poor conductors or

Department of Chemistry, Center for Materials Sciences and Nanotechnology, University of Oslo, P.O. Box 1033 Blindern, N-0315 Oslo, Norway. E-mail: ponniahv@kjemi.uio.no; Web: http://www.folk.uio.no/ponniahv

† Electronic supplementary information (ESI) available. See DOI: 10.1039/c3ra44248a

semiconductors.[6] According to the electronic structure calculations $SrAl_2H_2$ and SrAlSiH have metallic and semiconducting behavior respectively.[2] On the other hand present electronic structure calculations predict that $SrAl_2H_2$ is a narrow bandgap semiconductor. An essential issue in developing semiconductor devices for photovoltaics and thermoelectrics is to design materials with appropriate band gaps and with the dopant levels properly positioned with respect to the bands. Local density (LDA) and generalized gradient approximation (GGA) density functionals generally underestimate band gaps for semiconductors and sometimes incorrectly predict a metal. Hybrid functionals that include some exact Hartree–Fock exchange are known to be better, in particular B3LYP have been used successfully to describe many properties of a large variety of systems.[7–9] There is therefore an interest in applying hybrid functionals to the study of the present systems. The purpose of this article is to better elucidate the electronic structure, bonding nature, Raman and IR studies of these AB_2H_2 and *ABC*H (A = Sr, Ba; B = Al, Ga; C = Si, Ge) phases in detail.

Computational details

We employed DFT based methods, in particular, CASTEP,[10] as implemented in MATERIALS STUDIO 6.0 to optimize ionic positions and lattice parameters of all the compounds reported in the present article. For structural optimisation, Vanderbilt pseudopotentials[11] were utilized for all atoms together with a fine mesh of k points, with the energy conversion threshold of 0.01 eV per atom, maximum displacement of 0.001 Å and maximum force of 0.03 eV $Å^{-1}$, yielding high accurate energy and atomic displacements. The plane-wave cutoff energy of 600 eV is employed throughout the structural optimization calculation. The Perdew–Burke–Ernzerhof and the generalized gradient form (GGA-PBE)[12] of the exchange-correlation functional were applied. The electronic properties were computed by using the hybrid B3LYP[13] on the structures optimized at PBE level. Density functional perturbation theory (DFPT)[14] as implemented in CASTEP[10] was used for phonon calculations. For the band structure and phonon calculation we have used norm-conserving pseudopotentials with 850 eV energy cut-off for all atoms together with a $14 \times 14 \times 12$ mesh of k points, with the energy conversion threshold of 0.01 meV per atom. The reference configurations of valence electrons for the elements were Sr: $4s^2$, $4p^6$, $5s^2$; Ba: $5s^2$, $5p^6$, $6s^2$; Al: $3s^2$, $3p^1$; Ga: $4s^2$, $3d^{10}$, $4s^2$, $4p^1$; Si: $3s^2$, $3p^2$, Ge: $4s^2$, $4p^2$.

Structural details

Among the AB_2H_2 series only $SrAl_2H_2$, $BaGa_2H_2$, and $SrGa_2H_2$ phases are known experimentally. $BaAl_2H_2$, have not been observed experimentally, as all the synthesis attempts have proven so far to be unsuccessful.[15] In the present study we assume that $BaAl_2H_2$ also stabilize in a similar structure as the other iso-electronic compounds in the AB_2H_2 series. $SrAl_2H_2$, $BaGa_2H_2$, and $SrGa_2H_2$ are stabilizing in a hexagonal structure with space group $P\bar{3}m1$, as shown in Fig. 1. The B atoms are arranged as puckered graphitic layers where they have three nearest A neighbors, and the vacant coordination is taken by hydrogen. Thus, hydrogen appears to act as a pair of scissors cutting covalent B–B bonds and subsequently terminating them (Fig. 1c and d). The AB_2H_2 hydrides are electron precise Zintl phases. This retains a (two-dimensional) polyanionic structure $[B_2H_2]^{2-}$ in the hydride with both B–B and B–H bonds and is remarkable against the alanate structures which consist of tetrahedral $[AlH_4]$ or octahedral $[AlH_6]$ entities. In AB_2H_2 hydrides three crystallographic sites are occupied; A in 1a, B in 2d and one H atom located on another 2d site. The unit cell contains only one formula unit, *i.e.*, AB_2H_2. Each B atom is surrounded by one H atom and three B atoms at the equilibrium volume. The B atoms are making a network (6 rings) along the

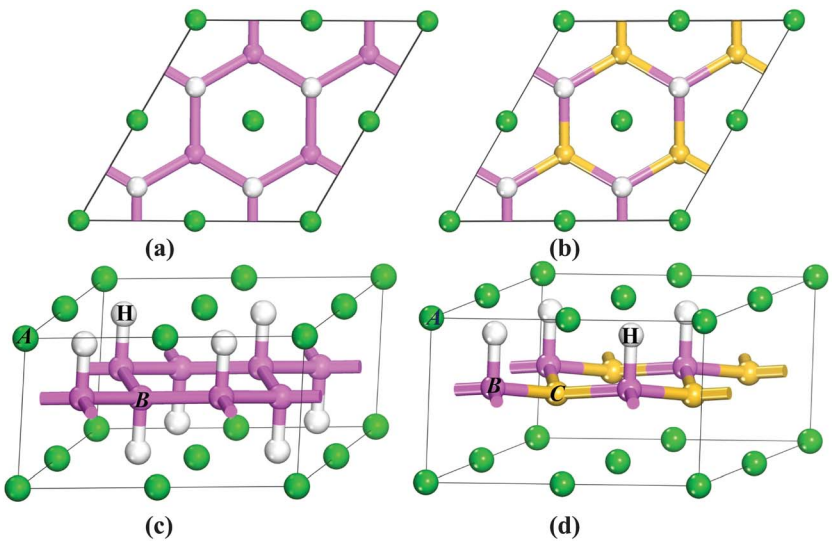

Fig. 1 Crystal structures of trigonal AB_2H_2 (a and c) and *ABC*H (b and d) (A = Sr, Ba; B = Al, Ga; C = Si, Ge): viewed along [001] (a and b) and [110] (c and d). The atomic label for the different kinds of atoms is given in the illustration.

ac plane and this structure can be considered as a layered structure as shown in Fig. 1c. Due to the H–H repulsive interaction of the negatively charged H ions, the networks are well separated. The *A* atoms are located in a sandwich-like manner in the space between these nets. Each *A* atom is surrounded by six H atoms.

The structure of *ABC*H (for example SrAlSiH) is very similar to that of AB_2H_2 series (see Fig. 1b and d) half of the *B*–H entities in the 2D polyanionic layer of AB_2H_2 are replaced by *C* atoms. This replacement occurs in a completely ordered way, that is, each *C* atom is surrounded by three *B*–H entities and *vice versa*. The center of inversion present in AB_2H_2 is lost in *ABC*H and the space-group symmetry is reduced to *P*3*m*1. The most conspicuous difference between the two structures is that the *A* atom in *ABC*H is only coordinated by three H atoms. Both compounds possess electron-precise polyanions $[B_2H_2]^{2-}$ and $[BCH]^{2-}$ with structures in accordance with the Zintl concept.

Results and discussion

In our theoretical simulation, we have relaxed the atomic positions and *c*/*a* globally using force-minimization technique fixed to experimental volume. Then the theoretical equilibrium volume is determined by varying the cell volume within ±10% of experimental volume. For the $BaAl_2H_2$ phase we have used the $BaGa_2H_2$ structural details are as an input and the forces as well as stress are relaxed globally. Finally the calculated energy *versus* volume data are fitted into the universal-equation-of-state fit and the equilibrium cell parameters are extracted. The theoretically obtained structural parameters and the positional parameters are presented along with experimental data in Table 1 and Table 2 (complete optimized structures are given in Table S1 and S2†) for AB_2H_2 and *ABC*H, respectively. From these tables it is clear that the equilibrium structural parameters obtained from our theoretical calculations are in very good agreement with the corresponding experimental findings. The calculated cell parameters are differing within 1.5% with the experimental values. Our computed Al–H distances in the $SrAl_2H_2$ is 1.72 Å, while the experimentally determined nearest-neighbor Al–H distances is 1.71 Å.[3] The calculated Al–H distances in AB_2H_2 phases vary from 1.70 (in $BaAl_2H_2$) to 1.72 (in $SrAl_2H_2$) Å. Similarly, the calculated Ga–H distances in *A*GaCH compounds range from 1.74 (in BaGaGeH) to 1.77 Å (in SrGaSiH) are good agreement with the experimental values (see Table S3 in the ESI†). The results presented in the rest of the manuscript are based on the theoretical equilibrium lattice parameters.

Electronic structure

The calculated total density of states and band structure for the $SrAl_2H_2$ with GGA-PBE level is given in Fig. 2. Our calculated total DOS and band structure for the $SrAl_2H_2$ are similar to previous theoretical findings. Near the Fermi energy, there are two bands of Al-p character that stay mostly below the Fermi level, but cross along Γ–A, leading to metallic character

Table 1 The calculated equilibrium structural parameters (*a* and *c* are in Å) and bandgap values for the AB_2H_2 (*A* = Sr, Ba; *B* = Al, Ga) phases

		Position (*z*)		
Compound	Cell parameters (Å)	*B*	H	Bandgap (E_g)
$SrAl_2H_2$	$a = 4.5471$ (4.5253)[a], $c = 4.7102$ (4.7214)[b]	0.4598 (0.4589)[b]	0.0955 (0.0976)[b]	0.324
$SrGa_2H_2$	$a = 4.4479$ (4.3932)[c], $c = 4.7057$ (4.6990)[b]	0.4628 (0.4656)[c]	0.1013 (0.1067)[c]	0.495
$BaAl_2H_2$[a]	$a = 4.6904$, $c = 4.9190$	0.4616	0.1157	0.356
$BaGa_2H_2$	$a = 4.5695$ (4.5286)[c], $c = 4.9089$ (4.8991)[c]	0.4688 (0.4680)[c]	0.1230 (0.1232)[c]	0.404

[a] Hypothetical phase; experimentally not yet identified. Optimised atomic coordinates of all these phases are given in Table S1 in the ESI. [b] From ref. 3. [c] From ref. 32.

Table 2 The calculated equilibrium structural parameters (*a* and *c* are in Å) and bandgap values for the *ABC*H (*A* = Sr, Ba; *B* = Al, Ga; *C* = Si, Ge) phases. The corresponding experimental values are given in parenthesis[a]

		Position (*z*)			
Compound	Cell parameters (Å)	*B*	*C*	H	Bandgap (E_g)
SrAlSiH	$a = 4.2971$ (4.2202)[b], $c = 4.8902$ (4.9662)[b]	0.5383, (0.5403)[b]	0.4465, (0.4451)[b]	0.8970, (0.8916)[b]	1.58
SrAlGeH	$a = 4.2683$ (4.2421)[c], $c = 4.9131$ (4.9691)[c]	0.5450, (0.5363)[c]	0.4368, (0.4481)[c]	0.8929, (0.8864)[c]	1.86
SrGaSiH	$a = 4.1943$ (4.1881)[e], $c = 4.9483$ (5.0025)[e]	0.5422, (0.5494)[e]	0.4391, (0.4444)[d]	0.9000, (0.9031)[d]	1.43
SrGaGeH	$a = 4.2722$ (4.2221)[d], $c = 4.9425$ (4.9691)[d]	0.5495, (0.5585)[d]	0.4257, (0.4402)[e]	0.9052, (0.9056)[e]	1.40
BaAlSiH	$a = 4.4004$ (4.3416)[e], $c = 5.1958$ (5.2929)[e]	0.5373, (0.5346)[e]	0.4568, (0.4582)[e]	0.8637, (0.8643)[e]	1.66
BaAlGeH	$a = 4.3901$ (4.3444)[c], $c = 5.1942$ (5.2115)[c]	0.5370, (0.5395)[c]	0.4512, (0.4551)[c]	0.8708, (0.8703)[c]	1.63
BaGaSiH	$a = 4.3218$ (4.3015)[d], $c = 5.1903$ (5.2703)[d]	0.5375, (0.5423)[d]	0.4485, (0.4555)[d]	0.8744, (0.8759)[d]	1.37
BaGaGeH	$a = 4.4040$ (4.3344)[d], $c = 5.1557$ (5.1895)[d]	0.5424, (0.5432)[d]	0.4380, (0.4437)[d]	0.8799, (0.8730)[d]	1.06

[a] Optimised atomic coordinates of all these phases are given in Table S2 in the ESI. [b] From ref. 2. [c] From ref. 32. [d] From ref. 4. [e] From ref. 33.

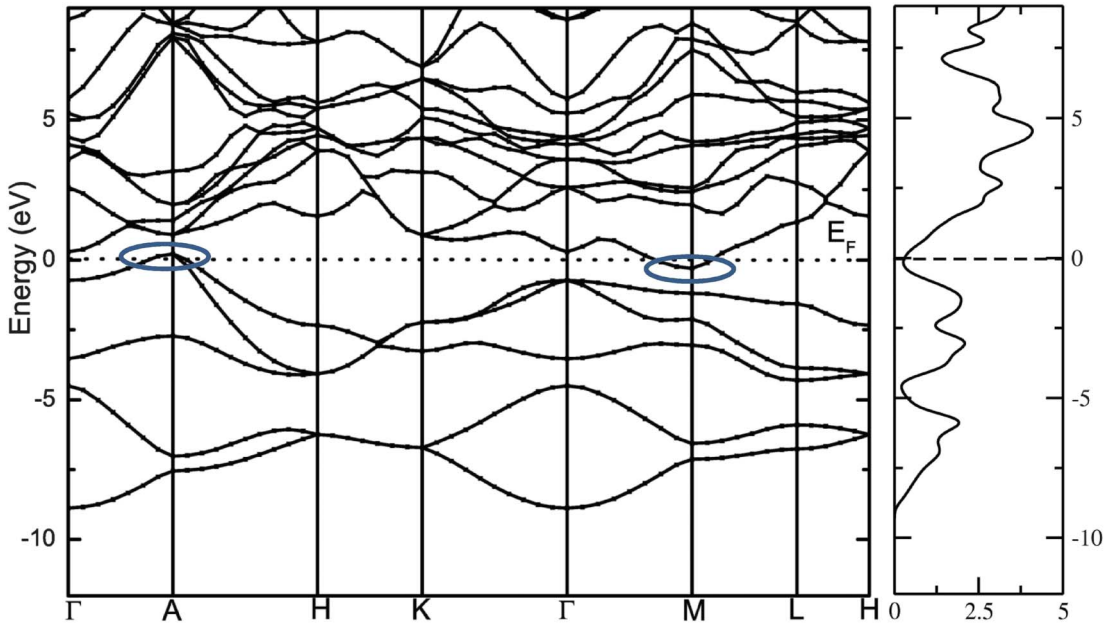

Fig. 2 Calculated electronic band structure and total DOS of $SrAl_2H_2$ with GGA and PW91 functional. The bands crossover at the top of the valence band and bottom of the conduction band at the Fermi level is highlighted as oval shape.

(see Fig. 2). In particular these two bands lead to hole in the Fermi surfaces around A, which are compensated by an electron pocket around M. It is well known that the bandgap (E_g) values of solids obtained from usual DFT calculations are systematically underestimated due to discontinuity in the exchange correlation potential. Thus the calculated E_g values are commonly 30–50% smaller than those measured experimentally.[16] It is commonly recognized that the theoretically calculated *e.g.* for semiconductors and insulators are strongly dependent on the approximations used and in particular on the exchange and correlation terms of the potential. It should be noted that in the AB_2H_2 compounds there is neither crossover nor nesting in between the valance band (VB) and conduction band (CB; see Fig. 2). This finding clearly indicates that the VB and CB are separated; but, due to the limitation in the computed GGA-PBE functional the E_g between the VB and CB is disappear/underestimated. On the other hand when we used hybrid B3LYP functional the obtained total DOS and band structure are almost similar to that of the GGA-PBE level but the VB and CB are separated by 0.324 eV (in $SrAl_2H_2$). In general, hybrid B3LYP functional gave more realistic bandgap value for wide range of materials. For example, $CuInSe_2$ has a band gap of 1.04 eV, but ordinary PBE and PW91 GGA predicts *e.g.* = 0.01 eV (LDA yield zero band gap)[17] while B3LYP gives[17] 0.95 eV that is very close to the experimental value.[18] Furthermore for La_2CuO_4 B3LYP exactly reproduces the experimental bandgap value 2.0 eV.[19] Theoretical and experimental studies of hydrides are mainly focused on acceleration of kinetics hydrogenation/dehydrogenation processes at moderate temperatures and on increase of the weight percentage of hydrogen. Since band gap of the compound is not the key parameter influencing on the above material properties, experimental measurements and hybrid DFT estimations of the parameter is limited and for most of the hydrides is not available. Heyd–Scuseria–Ernzerhof (HSE)[20] is another hybrid functional that has been used to estimate the band gap. It should be noted that the measured optical band gap value for α-MgH_2 is 5.6 eV[21] which is in good agreement with B3LYP (5.38 eV[22]) calculation, and not far from the corresponding value calculated by HSE06 (4.58 eV).[23] Similarly for the α-AlH_3 phase (no experimental value is available for comparison) the calculated band gap value at GW, HSE06, and B3LYP level are 3.54,[24] 3.38,[25] and 3.26[22] respectively, thus indicating that both HSE and B3LYP functionals give similar band gap value for AlH_3. Hence, we expect that the performance of the HSE functional in reproducing the band gap value for these AB_2H_2 and *ABC*H phases does not differ significantly from the B3LYP. Similarly, the other compounds in the AB_2H_2 series are also having non-metallic character (see Fig. 3 and Table 1). It should be noted that the calculated band structure using GGA-PBE and hybrid B3LYP functional yield almost a similar band structure except the splitting of the VB and CB (*i.e.*, B3LYP functional just pushed away VB and CB with respect to each other). The magnitude of the E_g and band positions suggests that the AB_2H_2 compounds are in-direct narrow bandgap semiconductors. It is worthy to note that a similar type of isoelectronic compound CaB_2H_2 has also having non-metallic character.[26] It is important to recall that these AB_2H_2 hydrides might be synthesized by first making the intermetallics followed by hydrogenation. The intermetallics can be made by arc melting although it is a little challenging since many of the components are quite volatile at high temperature. Even if these compounds are made with special techniques, it is hard to avoid the formation of impurities and secondary phases. This is the reason why the optical measurements on such type of materials are limited.

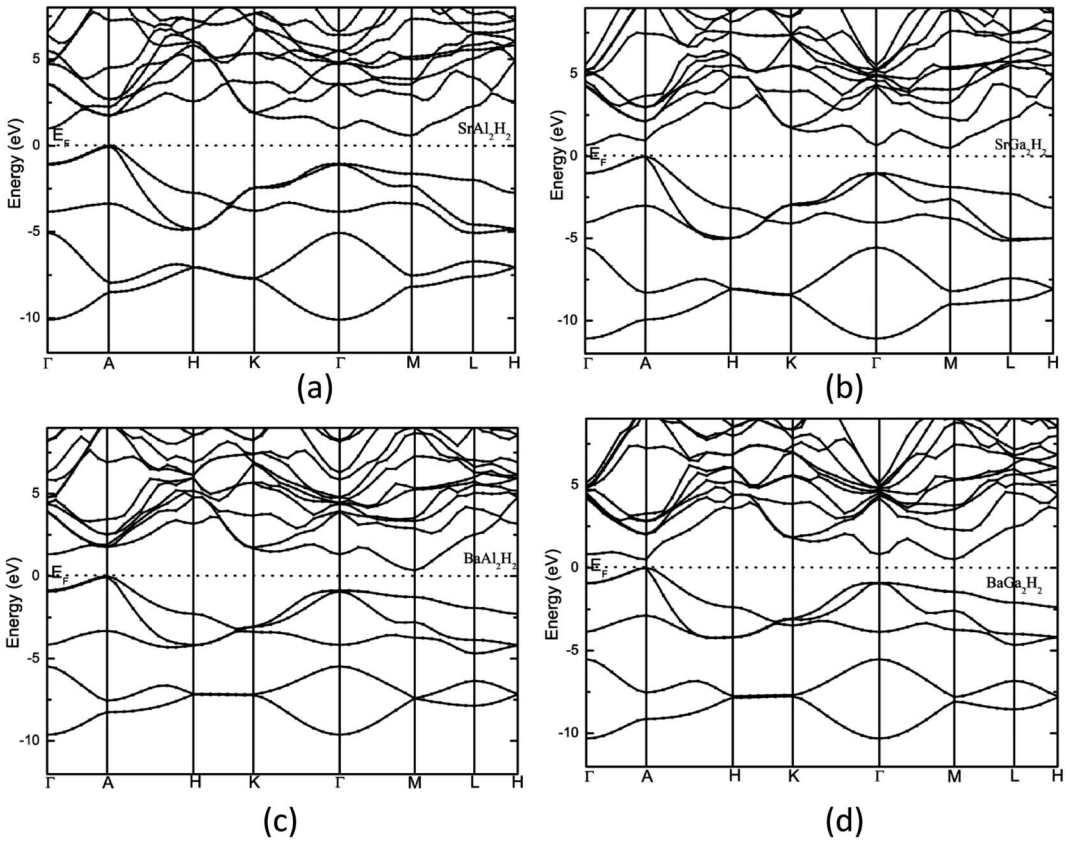

Fig. 3 Calculated electronic band structure of (a) $SrAl_2H_2$, (b) $SrGa_2H_2$, (c) $BaAl_2H_2$, and (d) $BaGa_2H_2$. The Fermi level is set to zero.

Owing to close similarity between the partial DOS (PDOS; computed using hybrid B3LYP functional) for the different members of the AB_2H_2 series (Fig. 4), we have documented only the findings for $SrAl_2H_2$. As seen from Fig. 4, the PDOS for Sr show very small contributions from s and p states in the VB.

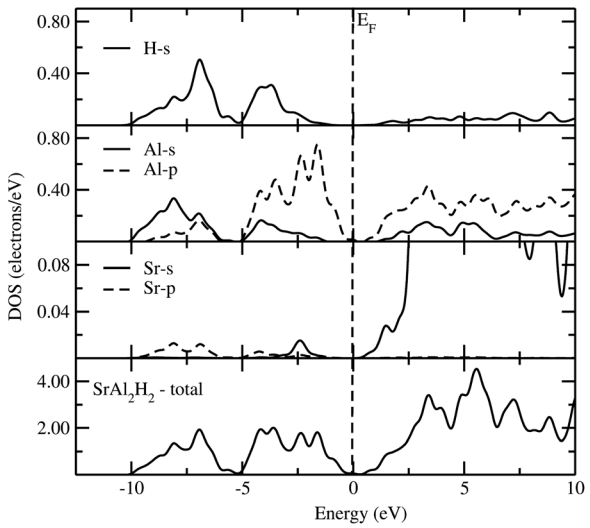

Fig. 4 Calculated total and partial DOS of $SrAl_2H_2$ using B3LYP functional. The Fermi level is set at zero energy and marked by the vertical dotted line.

This demonstrates that the valence electrons are transferred from the Sr sites to the Al and H sites. The partial DOS for Al shows that the s and p states of $SrAl_2H_2$ are well separated. The energetic separation of the Al-p and H-s facilitates the ionic bonding between Al and H, an inference that is further substantiated by the charge–density and charge transfer analysis. It should be important to note that in complex hydrides the interaction between the Al–H is mixed ionic and covalent bonding. Similar to the AB_2H_2 series, the calculated E_g of *ABC*H series are indirect and ranges between 1.06 and 1.86 eV. In general, aluminium hydrides seem to yield the largest E_g for polyanionic hydrides *ABC*H, the ones calculated for gallium hydrides. Again our calculated E_g value with hybrid B3LYP functional for the *ABC*H phases is much higher than the literature value. It should be noted that the experimentally observed E_g value for the SrAlSiH phase is 0.63 eV that is ~0.9 eV smaller than the present theoretical value. The possible reason is either the adopted theoretical approach is overestimating the bandgap value or the measured sample might have considerable impurities. As we noted in the previous para ordinary PBE always underestimate the bandgap. On the other hand, for the SrAlSiH compound the calculated E_g using ordinary PBE yields a value of 0.65 eV (for the PBE and B3LYP calculations a similar structural parameters was used), that is little higher than the experimentally observed one. In addition, the measured room-temperature resistivity of SrAlSiH is about 110 Ω cm,[2] which is much higher than the intrinsic room-temperature resistivity of Ge

(46 Ω cm; bandgap of 0.73 eV). Hence, one can expect higher bandgap value in SrAlSiH. In order to compare/validate our results independent optical measurements are required on these phases.

Spectroscopic studies

In general, the prepared samples from various methods often contain more than one phase (mixed phases), impurities, *etc.*, and in such situations we can use the theoretically simulated spectra such as Raman and IR to distinguish different phases within the sample. So, the theoretical studies on spectroscopic properties of materials will be complementary to experimental studies to characterize contaminated or multiphase samples. In connection with that we have simulated the Raman and IR spectra and NMR related parameters like isotropic chemical shielding (σ_{iso}), quadrupolar coupling constant (C_Q), and quadrupolar asymmetry parameter (η_Q) for AB_2H_2 and *ABC*H phases. Due to the symmetry changes both AB_2H_2 and *ABC*H phases have considerably different Raman and IR spectra. According to the symmetry analysis (crystal point group) the optical modes at the Γ point can be classified into the following symmetry species for AB_2H_2 ($P\bar{3}m1$) and *ABC*H ($P3m1$):

$$\Gamma_{AB2H2} = 2A_{1g}(\mathrm{R}) + 2E_g(\mathrm{R}) + 3A_{2u}(\mathrm{I}) + 3E_u(\mathrm{I})$$

$$\Gamma_{ABCH} = 4A_1(\mathrm{R}) + 4E(\mathrm{R}) + 4A_1(\mathrm{I}) + 4E(\mathrm{I})$$

where the notations of R and I mean Raman active mode and IR active mode, respectively. The letter A and E denotes the main displacements along z (stretching) and in-plane xy (bending), respectively. According to the symmetry analysis there are 4 Raman and 6 IR active modes for space group $P\bar{3}m1$, among them, only 4 IR modes are visible (higher intensity) for the AB_2H_2 phases. Similarly for the space group $P3m1$ there are 8 Raman and 8 IR modes are active among them 6 Raman and 6 IR modes are visible (higher intensity) for the *ABC*H phases. Theoretically simulated Raman and IR spectra for AB_2H_2 are shown in Fig. 5 and Fig. 6 respectively. The frequencies at the Γ point for the AB_2H_2 and *ABC*H phases are summarized in Table 3. One can download the simulated Raman and IR spectrum (both frequency and intensity) for these phases from our DFTBD web site.[22] The calculated Raman and IR spectra of AB_2H_2 and *ABC*H phases consist of three well separated regions; internal [Al–H/Ga–H] stretching (region1: frequency from 875 to 1500 cm^{-1} in both Raman and IR spectra) and bending (region2: 550 to 800 cm^{-1} in Raman; 350 to 850 cm^{-1} in IR) modes are clearly separated from external lattice modes (region3: bellow 300 cm^{-1} in both IR and Raman spectra). It may be noted that similar type of theoretical finding using direct method shows that for $NaAlH_4$ the calculated Raman frequencies are in good agreement with the experimental values within 5% error.[27,28] In general the calculated Raman active phonon frequency values are underestimated compared with corresponding experimental frequencies. In the simulated IR spectra (see Fig. 6) we have not identified any imaginary frequency for the AB_2H_2 and *ABC*H phases, thus indicating that all the studied phases are ground-state structures for these systems, or at least they are dynamically stable.[29] In particular according to our calculations, the $BaAl_2H_2$ phase, that has been not yet identified experimentally, might be stabilize in $P\bar{3}m1$. Hence, we need experimental verification to confirm our prediction.

The computation method for the NMR related parameters are well described in our previous article.[28] The calculated values of σ_{iso}, C_Q, and η_Q for both AB_2H_2 and *ABC*H phases are displayed in Table 4. The calculated σ_{iso} value for Sr atom scatters between 2725 and 4912 ppm, for the Ba atom scatters between 4823 and 5185 ppm, for Al atom scatters from 298 to 463, for Ga atom scatters from 803 to 1136, for Si atom scatters from 387 to 544 and for Ge atom scatters from 763 to 1808 ppm. It should be noted that the calculated σ_{iso} values cannot be compared directly to the experimental values, because, the

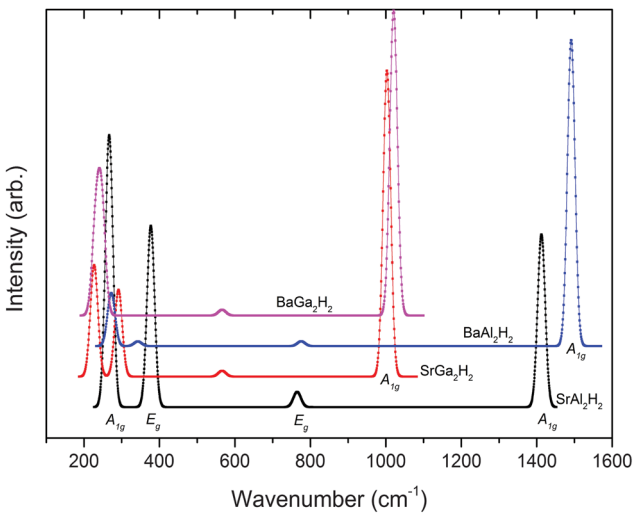

Fig. 5 Theoretically simulated Raman spectra for the AB_2H_2 phases at ambient conditions.

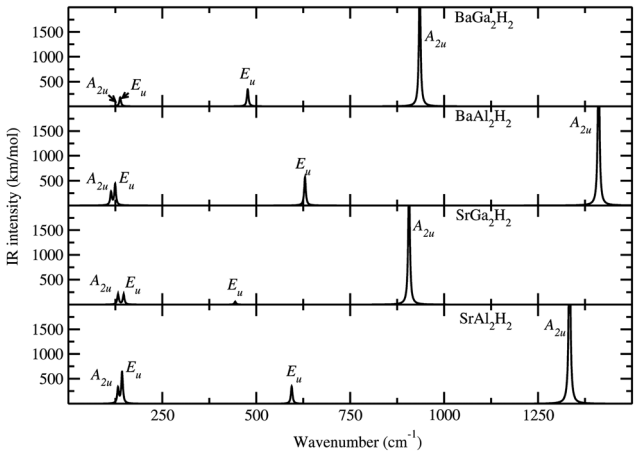

Fig. 6 Theoretically simulated IR spectra for the AB_2H_2 phases at ambient conditions. The corresponding modes are marked in the IR peak.

Table 3 The calculated Raman and IR frequency (in cm^{-1}) for the modes at the Γ point of the Brillouin zone for AB_2H_2 and ABCH (A = Sr, Ba; B = Al, Ga; C = Si, Ge) phases

Compound	Raman active modes	IR active modes
$SrAl_2H_2$	A_{1g}: 267, 1412. E_g: 377, 765	A_{2u}: 132, 1333. E_u: 143, 593
$SrGa_2H_2$	A_{1g}: 223, 1003. E_g: 291, 564	A_{2u}: 161, 898. E_u: 176, 351
$BaAl_2H_2$	A_{1g}: 272, 1491. E_g: 343, 776	A_{2u}: 108, 1406. E_u: 124, 623
$BaGa_2H_2$	A_{1g}: 231, 1020. E_g: 246, 566	A_{2u}: 168, 934. E_u: 141, 410
SrAlSiH	A_1: 154, 231, 1233. E: 150, 422, 819	A_1: 154, 231, 1233 (1211[a], 1220[b]). E: 150, 422, 819 (870[a])
SrAlGeH	A_1: 112, 216, 928. E: 122, 351, 557	A_1: 112, 216, 918. E: 122, 351, 557
SrGaSiH	A_1: 134, 191, 786. E: 123, 342, 582	A_1: 134, 191, 786. E: 123, 342, 582
SrGaGeH	A_1: 110, 147, 809. E: 111, 244, 547	A_1: 110, 147, 809. E: 111, 244, 547
BaAlSiH	A_1: 130, 224, 1278. E: 129, 378, 818	A_1: 130, 224, 1278 (1220[c]). E: 129, 378, 818
BaAlGeH	A_1: 100, 199, 1306. E: 110, 321, 809	A_1: 100, 199, 1306 (1240[b]). E: 110, 321, 809
BaGaSiH	A_1: 122, 170, 1119. E: 110, 317, 840	A_1: 122, 170, 1119. E: 110, 317, 840
BaGaGeH	A_1: 96, 127, 1152. E: 97, 226, 789	A_1: 96, 127, 1152. E: 97, 226, 789

[a] From ref. 34. [b] From ref. 35. [c] From ref. 36.

Table 4 Computed NMR parameters such as isotropic chemical shielding (σ_{iso}; in ppm), quadrupolar coupling constant (C_Q; in MHz), and quadrupolar asymmetry (η_Q) parameters for AB_2H_2 and ABCH (A = Sr, Ba; B = Al, Ga; C = Si, Ge) phases

	NMR	
Compound	σ_{iso} (ppm)	CQ (MHz)
$SrAl_2H_2$	Sr: 2894, Al: 463	Sr: 9.6, Al: 6.9
$SrGa_2H_2$	Sr: 4912, Ga: 803	Sr: 1.8, Ga: 9.5
$BaAl_2H_2$	Ba: 5185, Al: 407	Ba: 23.5, Al: 6.7
$BaGa_2H_2$	Ba: 4823, Ga: 834	Ba: 23.7, Ga: 8.8
SrAlSiH	Sr: 2766, Al: 363, Si: 544	Sr: 18.6, Al: 7.2 (7.5[a]), Si: 22.2
SrAlGeH	Sr: 2773, Al: 344, Ge: 1808	Sr: 17.7, Al: 7.7, Ge: 9.9
SrGaSiH	Sr: 2725, Ga: 1136, Si: 391	Sr: 24.3, Ga: 13.4, Si: 65.7
SrGaGeH	Sr: 2759, Ga: 852, Ge: 763	Sr: 22.8, Ga: 9.4, Ge: 26.4
BaAlSiH	Ba: 5036, Al: 313, Si: 418	Ba: 20.8, Al: 7.2, 31.7
BaAlGeH	Ba: 5062, Al: 289, Ge: 1458	Ba: 21.5, Al: 7.5, Ge: 14.9
BaGaSiH	Ba: 4980, Ga: 943, Si: 387	Ba: 25.3, Ga: 8.0, Si: 79
BaGaGeH	Ba: 4978, Ga: 892, Ge: 252	Ba: 27.6, Ga: 8.4, Ge: 33.2

[a] From ref. 2.

calculated values correspond to absolute chemical shielding, whereas, most experimental σ_{iso} values are usually reported with shifts relative to a known standard. However, the direct comparison between experiment and theory can be made on comparative shifts between the different peaks. Similarly, the C_Q and η_Q values are also scattered in wide range (see Table 4) and these values are directly comparable with experimental values. From Table 4 it is evident that the calculated and experimentally observed C_Q value for Al in the SrAlSiH phase is in good agreement with each other. In general, the theoretically predicted values are always lower than the experimental values for the C_Q and η_Q. It should be noted that present type of approach is not suitable for metallic systems (for more details, see ref. 30). In general, the NMR parameters are strongly related to the atomic environment (near neighbors) and quadrupolar coupling constants are directly related to the bond strength and the anisotropy in the charge density distribution around the probe nuclei. For example, due to the local environment change the calculated C_Q value for Al in the SrAlSiH is higher than that in the $SrAl_2H_2$. We believe that the present study can motivate experimentalists to perform NMR measurements for the AB_2H_2 and the ABCH phases.

Chemical bonding

The AB_2H_2 and the ABCH phases exhibit similar features and therefore we only document the charge density and the charge transfer plots (charge density difference between the crystalline – superposed atomic charge density) for $SrAl_2H_2$ and SrAlSiH. Fig. 7a–d shows the charge-density distribution at the Sr, Al, Si and H sites, from which it is evident that the highest charge density resides in the immediate vicinity of the nuclei. Further, the spherical charge distribution shows that the bonding interactions between Sr–H and Sr–Al have predominantly ionic character. On the other hand, the interactions between Al–H, Al–Al and Al–Si are rather directional. The substantial difference in the electro-negativity between Sr and Al/H suggests the presence of strong ionic character (*i.e.*, the Sr valence electrons transferred to the H/Al sites) and the small difference in the electronegativity between Al and H suggests the presence of strong covalent character. The polar character of both compounds is revealed in the charge transfer map, which clearly shows the charge depletion around Sr and accumulation between the Al–Al/Si–Al and H atoms. Concerning the Al–H bond, charge transfer plot (Fig. 7e–h) suggests substantial charge accumulation around the position of the H.

In order to quantify the bonding and estimate the amount of electrons on and between the participating atoms we have made Mulliken-population analysis. Although there is no unique definition to identify how many electrons are associated with an atom in a molecule or an atomic grouping in a solid, it has nevertheless proved useful in many cases to perform population analyses.[31] However, the method is more qualitative than quantitative, providing results that are sensitive to the atomic basis. The calculated Mulliken charges are reported in Table 5 for AB_2H_2 and ABCH phases. For the studied AB_2H_2 and ABCH phases the Mulliken effective charge (MEC) value for the A site is around $+1e$, B site is around $-0.2e$, and H is around $-0.3e$. This

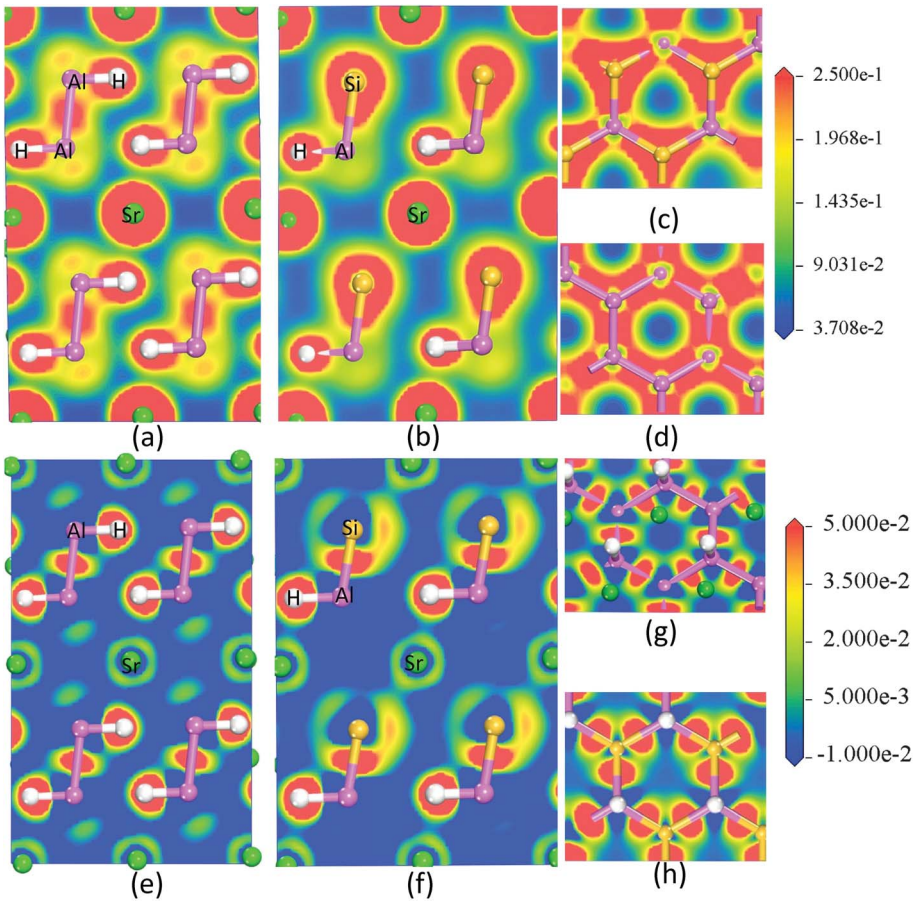

Fig. 7 The calculated valence electron charge density distribution (a, b, c and d) and charge transfer plot (e, f, g and h) for the $SrAl_2H_2$ and SrAlSiH phase in [111] plane.

finding is consistent with the charge density analyzes and the magnitude of the MEC shows that *A* does not completely donate its two valence electrons to the *B*/*C* and H atoms, which is much smaller than that in a pure ionic picture.

To understand the bond strength between the constituents the bond overlap population (BOP) values are calculated on the basis of Mulliken population analysis. The BOP values can provide useful information about the bonding property between atoms. A high BOP value indicates a strong covalent bond, while a low BOP value indicates an ionic interaction. The calculated BOP values for the AB_2H_2, *ABC*H phases are displayed in Table 5 and the corresponding interatomic distances are given in Table S3.† In the AB_2H_2 and the *ABC*H phases the BOP associated with the *A*–H bonds vary from 0.02 to 0.23 (minimum in BaAlSiH and maximum in $BaGa_2H_2$). Similarly, the calculated BOP varies for the *B*–H bonds from 0.21 to 0.62 (minimum in BaGaGeH and maximum in $SrAl_2H_2$), and for the *B*–*B* bonds from 1.1 to 2.2 (minimum in $BaGa_2H_2$ and maximum in $SrAl_2H_2$), and for the *B*–*C* bonds from

Table 5 Mulliken-population charge density analysis and bond overlap population (BOP) for AB_2H_2 and *ABC*H (*A* = Sr, Ba; *B* = Al, Ga; *C* = Si, Ge) phases. The Mulliken-effective charges (MEC) are given in terms of *e*

Compound	MEC	BOP
$SrAl_2H_2$	Sr: 1.17, Al: −0.26, H: −0.32	2.2 (Al–Al), 0.62 (Al–H), 0.11 (Sr–H)
$SrGa_2H_2$	Sr: 1.01, Ga: −0.22, H: −0.29	1.36 (Ga–Ga), 0.49 (Ga–H), 0.22 (Sr–H)
$BaAl_2H_2$	Ba: 1.19, Al: −0.25, H: −0.34	2.17 (Al–Al), 0.61 (Al–H), 0.04 (Ba–H)
$BaGa_2H_2$	Ba: 1.05, Ga: −0.22, H: −0.30	1.10 (Ga–Ga), 0.40 (Al–H), 0.23 (Ba–H)
SrAlSiH	Sr: 1.05, Si: −0.74, Al: 0.06, H: −0.37	2.34 (Al–Si), 0.6 (Al–H), 0.1 (Sr–H)
SrAlGeH	Sr: 0.91, Al: 0.08, Ge: −0.6, H: -0.37	1.99 (Al–Ge), 0.53 (Al–H), 0.12 (Sr–H)
SrGaSiH	Sr: 0.96, Ga: 0.16, Si: −0.49, H: −0.31	2.11 (Si–Ga), 0.48 (Ga–H), 0.13 (Sr–H)
SrGaGeH	Sr: 0.94, Ga: −0.19, Ge: −0.43, H: −0.31	1.93 (Ga–Ge), 0.26 (Ga–H), 0.15 (Sr–H)
BaAlSiH	Ba: 1.02, Al: 0.07, Si: −0.71, H: −0.37	2.34 (Si–Al), 0.52 (Al–H), 0.02 (Ba–H)
BaAlGeH	Ba: 0.88, Al: 0.07, Ge: −0.56, H: −0.38	2.04 (Ge–Al), 0.58 (Al–H), 0.15 (Ba–H)
BaGaSiH	Ba: 0.93, Ga: −0.12, Si: −0.49, H: −0.32	2.15 (Ga–Si), 0.34 (Ga–H), 0.20 (Ba–H)
BaGaGeH	Ba: 0.93, Ga: −0.21, Ge: −0.40, H: −0.32	1.10 (Ga–Ge), 0.21 (Ga–H), 0.18 (Ba–H)

1.10 to 2.34 (minimum in BaGaGeH and maximum in both SrAlSiH and BaAlSiH). These findings clearly demonstrates that the atomic size place an important role (*i.e.*, when the atomic-size/bond-length is increased the BOP value become degrease) and one can change/tune the covalent character by introducing Si/Ga or Ge in the $SrAl_2H_2$ matrix. Our BOP study clearly indicates that the directional bonding interaction is reduced when we move from Al to Ga based phases. The possible reason is that the outermost electrons in Ga are more diffuse in nature than that in Al. In general, the bonding interaction is completely changed when we move from top to the bottom of the Periodic table; for example: the electronic structure of IVa group elements (C, Si, Ga, Sn and Pb) of the Periodic table changes from insulator-to-semiconductor-to-metal (the outermost electrons in C are less diffuse in nature than that in the Pb case). In this AB_2H_2 and *ABC*H phases, the *A*–H bonds have dominant ionic character, whereas the *B*–H, and *B*–*B*/*B*–*C* interactions have noticeable covalent character. This finding is again consistent with our charge transfer and electronegativity difference analysis. When we compare the BOP values for the different bonding interaction between atoms in AB_2H_2 and *ABC*H phases, the *B*–*B*/*B*–*C* bonding interactions are overall much stronger.

Conclusion

The electronic structure, chemical bonding, and spectroscopic properties of AB_2H_2, and *ABC*H (A = Sr, Ba; B = Al, Ga; C = Si, Ge) phases have been studied by state-of-the-art density-functional calculations. Electronic structures calculations using B3LYP reveal that the AB_2H_2 phases are indirect narrow-bandgap semiconductors with estimated bandgap value varying between 0.324 and 0.495 eV. Similar to the AB_2H_2 series, the calculated bandgap value of *ABC*H series are indirect and have a size between 1.06 and 1.86 eV, *i.e.* much higher than the AB_2H_2 phases. The calculated IR and NMR parameters agree very-well with the available experimental values for the SrSiAlH phase. For further experimental investigations, we have simulated the Raman and IR spectra, and calculated the NMR related parameters (isotropic chemical shielding, quadrupolar coupling constant, and quadrupolar asymmetry) for the rest of the compounds. The chemical bonding character of these phases is analysed using DOS, charge density, charge transfer, and Mulliken population and found that the interactions between *B*–*B*/*B*–*C* and *B*–H have dominant covalent character and while interaction between *A*–H is dominantly ionic.

Acknowledgements

The authors gratefully acknowledge the Research Council of Norway (Grant no: 143408) for financial support. PV acknowledges the Research Council of Norway for providing the computer time at the Norwegian supercomputer facilities (Abel.uio.no) and Dr. M. F. Iozzi for fruitful discussions.

References

1 S. Z. Karazhanov, A. G. Ulyashin, P. Ravindran and P. Vajeeston, *Europhys. Lett.*, 2008, **82**, 17006.
2 T. Bjorling, D. Noreus, K. Jansson, M. Andersson, E. Leonova, M. Eden, U. Halenius and U. Haussermann, *Angew. Chem., Int. Ed.*, 2005, **44**, 7269–7273.
3 F. Gingl, T. Vogt and E. Akiba, *J. Alloys Compd.*, 2000, **306**, 127–132.
4 M. J. Evans, G. P. Holland, F. J. Garcia-Garcia and U. Haeussermann, *J. Am. Chem. Soc.*, 2008, **130**, 12139–12147.
5 M. J. Evans, Y. Wu, V. F. Kranak, N. Newman, A. Reller, F. J. Garcia-Garcia and U. Häussermann, *Phys. Rev. B: Condens. Matter Mater. Phys.*, 2009, **80**, 064514.
6 S. C. Sevov, *Zintl Phases in Intermetallic Compounds, Principles and Practice: Progress*, John Wiley & Sons. Ltd., Chichester, England, 2002, pp. 113–132.
7 S. Kümmel and L. Kronik, *Rev. Mod. Phys.*, 2008, **80**, 3–60.
8 M. Marsman, J. Paier, A. Stroppa and G. Kresse, *J. Phys.: Condens. Matter*, 2008, **20**, 064201.
9 J. Paier, M. Marsman and G. Kresse, *J. Chem. Phys.*, 2007, **127**, 024103.
10 S. J. Clark, M. D. Segall, C. J. Pickard, P. J. Hasnip, M. I. J. Probert, K. Refson and M. C. Payne, *Z. Kristallogr.*, 2005, **220**, 567–570.
11 D. Vanderbilt, *Phys. Rev. B: Condens. Matter*, 1990, **41**, 7892–7895.
12 J. P. Perdew, K. Burke and M. Ernzerhof, *Phys. Rev. Lett.*, 1996, **77**, 3865–3868.
13 A. D. Becke, *J. Chem. Phys.*, 1993, **98**, 5648–5652.
14 K. Refsen, S. J. Clark and P. R. Tulip, *Phys. Rev. B: Condens. Matter Mater. Phys.*, 2006, **73**, 155114.
15 D. Moser, U. Häussermann, T. Utsumi, T. Björling and D. Noréus, *J. Alloys Compd.*, 2010, **505**, 1–5.
16 *Theory of the Inhomogeneous Electron Gas*, ed. S. Lundqvist and N. H. March, Springer, Plenum, New York, 1983.
17 H. Xiao, J. Tahir-Kheli and W. A. Goddard, *J. Phys. Chem. Lett.*, 2011, **2**, 212–217.
18 J. L. Shay, B. Tell, H. M. Kasper and L. M. Schiavone, *Phys. Rev. B: Solid State*, 1973, **7**, 4485–4490.
19 J. K. Perry, J. Tahir-Kheli and W. A. Goddard, *Phys. Rev. B: Condens. Matter*, 2001, **63**, 144510.
20 J. Heyd, G. E. Scuseria and M. Ernzerhof, *J. Chem. Phys.*, 2003, **118**, 8207–8215.
21 J. Isidorsson, I. A. M. E. Giebels, H. Arwin and R. Griessen, *Phys. Rev. B: Condens. Matter*, 2003, **68**, 115112.
22 P. Vajeeston and H. Fjellvåg, *Density Functional Theory Based Database (DFTBD)*, http://folk.uio.no/ponniahv/Database, University of Oslo, Norway, 2013.
23 T. Adit Maark, T. Hussain and R. Ahuja, *Int. J. Hydrogen Energy*, 2012, **37**, 9112–9122.
24 M. J. van Setten, V. A. Popa, G. A. de Wijs and G. Brocks, *Phys. Rev. B: Condens. Matter Mater. Phys.*, 2007, **75**, 035204.
25 L. Ismer, A. Janotti and C. G. Van de Walle, *J. Alloys Compd.*, 2011, **509**, S658–S661, Supplement 2.
26 P. Vajeeston, P. Ravindran, B. C. Hauback and H. Fjellvåg, *Int. J. Hydrogen Energy*, 2011, **36**, 10149–10158.
27 X. Ke, A. Kuwabara and I. Tanaka, *Phys. Rev. B: Condens. Matter Mater. Phys.*, 2005, **71**, 184107.
28 P. Vajeeston, P. Ravindran and H. Fjellvåg, *J. Phys. Chem. A*, 2011, **115**, 10708–10719.

29 P. Souvatzis, O. Eriksson, M. I. Katsnelson and S. P. Rudin, *Phys. Rev. Lett.*, 2008, **100**, 095901.
30 C. J. Pickard and F. Mauri, *Phys. Rev. B: Condens. Matter*, 2001, **63**, 245101.
31 R. S. Mulliken, *J. Chem. Phys.*, 1955, **23**, 1833.
32 V. F. Kranak, M. J. Evans, L. L. Daemen, T. Proffen, H. M. Lee, O. F. Sankey and U. Haeussermann, *Solid State Sci.*, 2009, **11**, 1847–1853.
33 M. H. Lee, M. J. Evans, L. L. Daemen, O. F. Sankey and U. Haeussermann, *Inorg. Chem.*, 2008, **47**, 1496–1501.
34 M. H. Lee, O. F. Sankey, T. Bjorling, D. Moser, D. Noreus, S. F. Parker and U. Haussermann, *Inorg. Chem.*, 2007, **46**, 6987–6991.
35 V. F. Kranak, M. J. Evans, L. L. Daemen, T. Proffen, M. H. Lee, O. F. Sankey and U. Häussermann, *Solid State Sci.*, 2009, **11**, 1847–1853.
36 L. M. H. T. Bjoerling, B. C. Hauback, T. Utsumi, D. Moser, D. Bull, D. Noreus, O. F. Sankey and U. Haeussermann, *Phys. Rev. B: Condens. Matter Mater. Phys.*, 2008, **78**, 195209.